



# Fracture network mapping using Landsat-8 OLI, Sentinel-2A, ASTER, and ASTER-GDEM data, in the Rich area (Central High Atlas, Morocco)

Ibtissame Bentahar<sup>1</sup> · Mohammed Raji<sup>1</sup> · Hicham Si Mhamdi<sup>2</sup>

Received: 17 May 2020 / Accepted: 16 July 2020 / Published online: 8 August 2020  
© Saudi Society for Geosciences 2020

## Abstract

Geological mapping using remote sensing is one of the most important applied methods in natural resources exploration. The objectives of this study are mapping and analyzing of fractures distribution in the Rich area in order to understand the influence of lithology and geodynamics on fracture density. For this purpose, we relied on automatic lineament extraction using four types of satellite imagery: Landsat OLI, Sentinel 2A, ASTER L1B, and ASTER Global Digital Elevation Model (GDEM) in order to extract the maximum of lineaments affirmed significative in structural interpretations. After image corrections, the processing of these images is based on the highlighting of structural lineaments and their automatic extraction using the algorithm line of Geomatica software. The validation of linear structures was made based on existing data. The finding showed that each produced map shows systematically a similarity in terms of concentration and orientation with three preferential system-oriented NE-SW, NEE-SSW, E-W, and NNE-SSW. Lineaments mainly follow that of major fault zones, with a high concentration in the North-East part of the study area. This might be due to the importance of the Alpine orogeny deformation as well as the diapirism phenomenon of the Triassic formations in the hiner zone of the Atlas belt. However, the observation shows that the number and total length of structural lineaments could be extracted by using the sentinel 2A then Landsat OLI, ASTER-GDEM, and ASTER L1B set. The automatic extraction allows better mapping of structural lineaments. It shows a good agreement and more information compared with previous geological data, confirming the efficiency of applied techniques in geological studies.

**Keywords** Central High Atlas · Structural lineaments · Remote sensing · Automatic lineament extraction

## Introduction

Structural mapping is a presentation of the different structures on the Earth's surface, including linear structural features (fold axis, faults...). Mapping these structures allows understanding the dynamics of the movements of the Earth's crust. Moreover, mapping of structural lineaments is important in geological exploration because it shows the flow of fluid through in these fractures, analysis of these fractures is used

to discover reservoirs of groundwater and mineral deposits, and petroleum, as well as to understand the dynamics of the study area (Gad and Kusky 2007; Hamdani 2019; Kumar and Bhandary 2015). Conventional methods used in mapping structural lineaments do not detect all lineaments present in the study area. The integration of remote sensing in structural lineament mapping has contributed to improving the quality of the maps. In which it revealed the abundance of linear structures and significantly improved the knowledge of the study areas, as well as this method is very applicable in areas of difficult access and mountainous.

The lineament extraction using remote sensing can be grouped into automatic extraction where the extraction is performed by the algorithm based on enhancements including edge detection and filters then extraction (Adiri et al. 2017; Si Mhamdi et al. 2016). The manual extraction or visual inspection is performed by tracing manually by users on the color composites or band ratios of datasets or using directional filters that enhance the edge (El Alaoui El Moujahid et al. 2016; Kassou et al. 2012).

---

Responsible Editor: Biswajeet Pradhan

---

✉ Ibtissame Bentahar  
bentaharibtissame@gmail.com

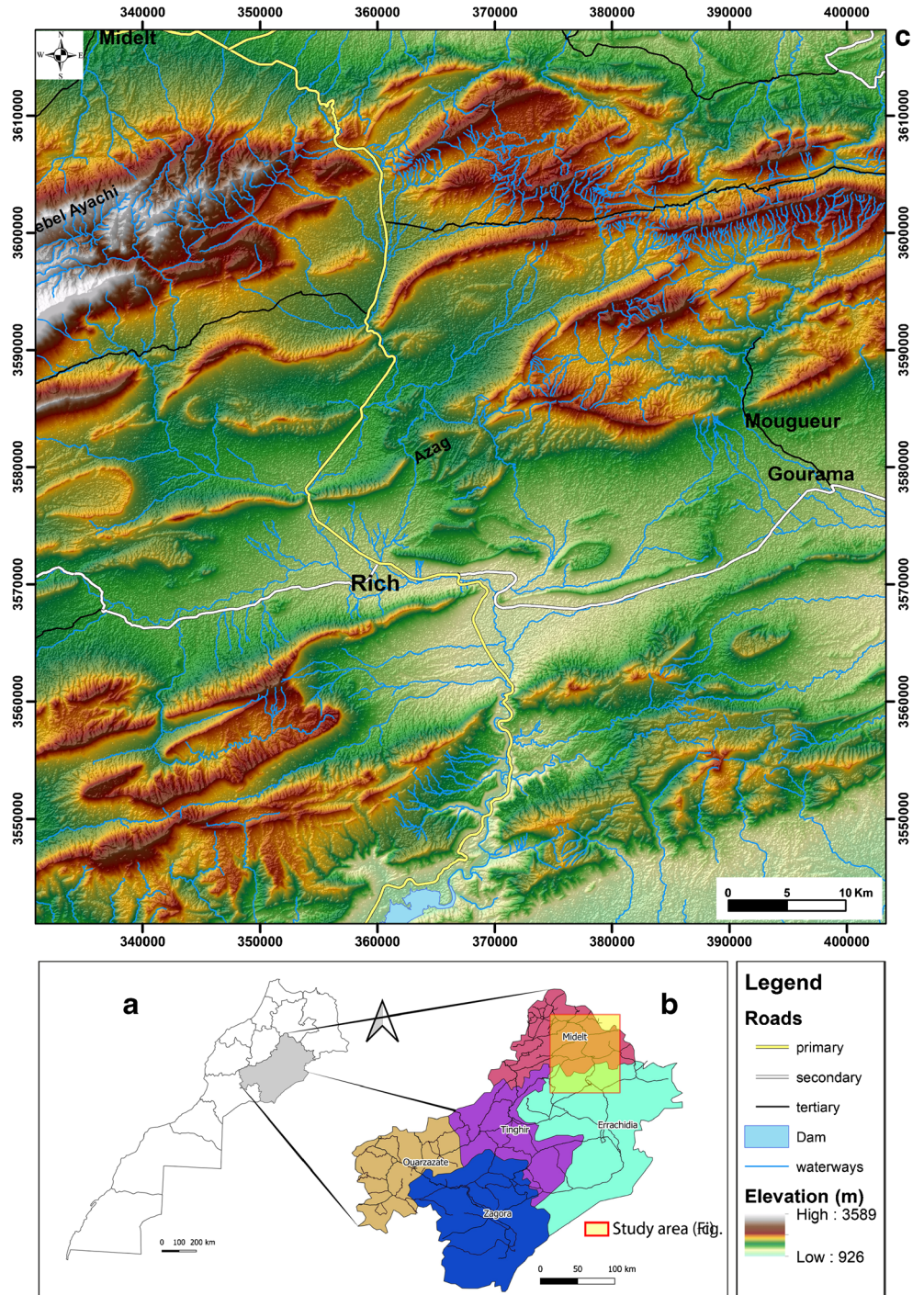
<sup>1</sup> Laboratory of Geodynamics of Old Belts, Department of Geology, Faculty of Sciences Ben M'Sik, Hassan II University of Casablanca, Casablanca, Morocco

<sup>2</sup> Department of Geosciences, Faculty of Sciences and Techniques Errachidia, University Moulay Ismail of Meknes, Meknes, Morocco

In the Atlas system, remote sensing techniques have been employed by Nouayti et al. (2017) using manual extractions covering a part of the study area. Other works investigated the potential of remote sensing using automatic or manual extraction elsewhere in the Atlas system, in the Western High Atlas (Si Mhamdi et al. 2017), and in the Central High Atlas (El Alaoui El Moujahid et al. 2016). Applied techniques show the importance of remote sensing in geological investigations.

In this study we investigate in the Errachidia-Midelt area, one of the key sectors in the Atlas system (Figs. 1 and 2). The study area is located along the National road Errachidia midelt. It is characterized by an abundance of brittle deformation as thrust fault and the related folding (Fig. 2), which are mainly in the Jurassic limestones that can reach up to 1000 m thick (Arboleya et al. 2004). This work is relevant to study the fracturing in the study area where fracturing is well developed,

**Fig. 1** Location of the study area: **A** Morocco, **B** Les provinces de la region des Deraa Tafilalet, and **C** topographic map of the study area



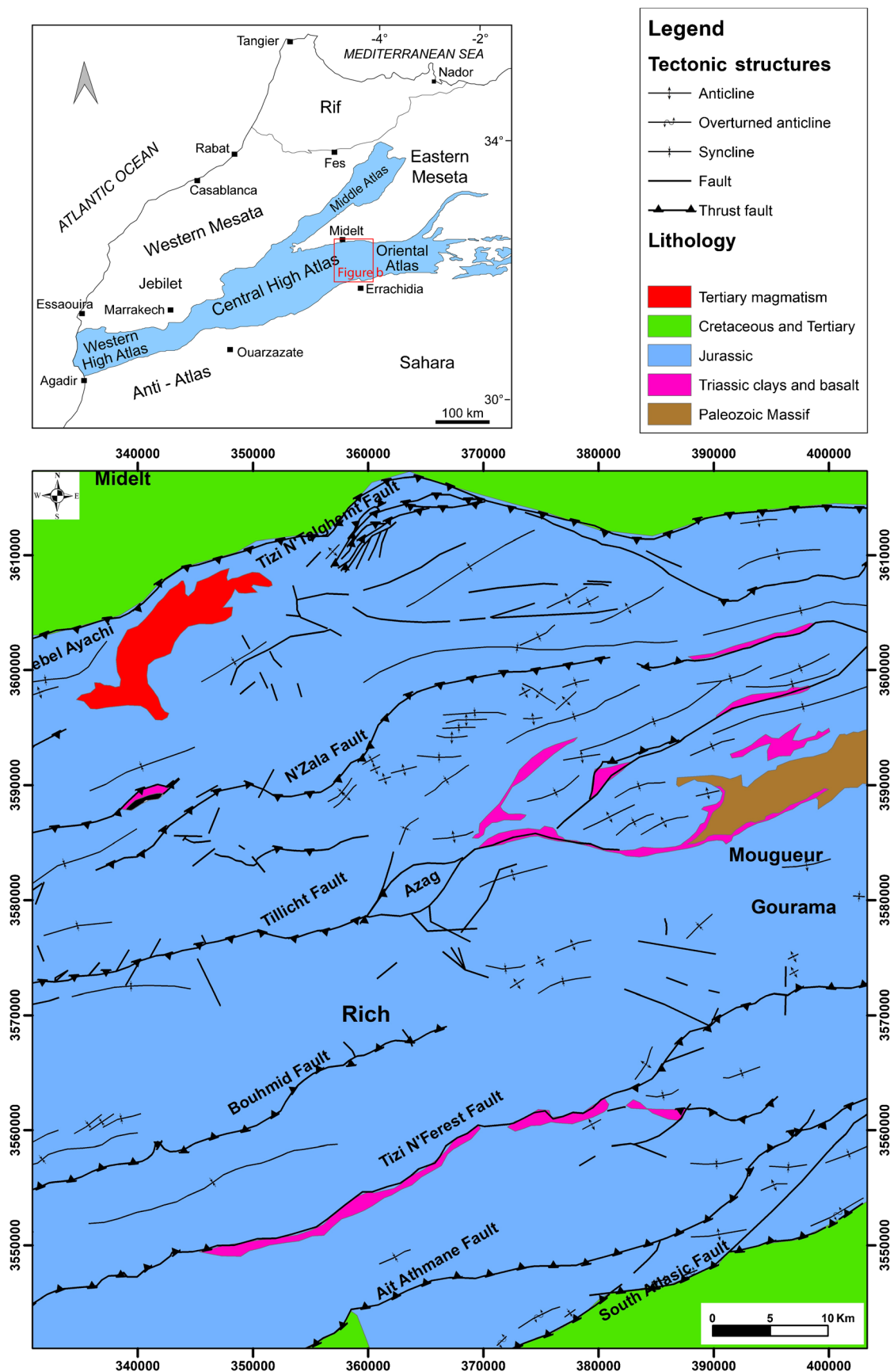


Fig. 2 Structural map of Rich area modified from Ibouh (2004)

**Table 1** Spectral bands of used data in this study

Landsat OLI			ASTER			Sentinel 2A		
Bands	Wavelength ( $\mu\text{m}$ )	Resolutions	Bands	Wavelength ( $\mu\text{m}$ )	Resolution	Bands	Wavelength ( $\mu\text{m}$ )	Resolutions
1	0.44	30 m	1	0.56	15 m	1	0.443	60 m
2	0.48	30 m	2	0.66	15 m	2	0.49	10 m
3	0.56	30 m	3N	0.82	15 m	3	0.56	10m
4	0.655	30 m	3B	0.82	15 m	4	0.665	10 m
5	0.865	30 m	4	1.65	30 m	5	0.705	20 m
6	1.61	30 m	5	2.165	30 m	6	0.74	20 m
7	2.2	30 m	6	2.205	30 m	7	0.783	10 m
8	0.59	15 m	7	2.26	30 m	8	0.842	20 m
9	1.37	30 m	8	2.33	30 m	8A	0.865	60 m
			9	2.395	90 m	9	0.945	60 m
						10	1.375	20 m
						11	1.610	20 m
						12	2.190	20 m

because it is affected by different tectonic phases of the alpine orogeny (Babault et al. 2013; Teixell et al. 2017).

We apply remote sensing techniques to different data to extract lineaments automatically, due to the difficulty of access in some areas and the geographic extent of the study zone; the use of conventional methods in fracture mapping is difficult to identify all existing lineaments and follow fault extension.

Besides the identification of geological structures and the interpretation to determine the geological factors (lithological and dynamic) controlling the distribution of structural lineaments in the study areas, another purpose of this study is to evaluate the efficiency of different datasets (Landsat OLI, Sentinel 2A, ASTER, and ASTER-GDEM) to detect structural lineaments automatically that were not identified in previous work in order to develop a well-detailed fracture map. The results obtained are supported by pre-existing geological data integrated in a Geographic Information System (GIS) (Oo et al. 2019). Four main systems were identified: NE-SW, NEE-SSW, E-W, and NNE-SSW: all structures are related to alpine shortening. The finding will be a useful reference to understand the geodynamics of this region, as well as to improve the structural knowledge of the Central High Atlas, moreover, for future mineralogical and hydrological exploration as well as infrastructure engineering (Bednarik 2019; Dormishi et al. 2018; Mafi Gholami and Baharlouii 2019)

## Geological setting

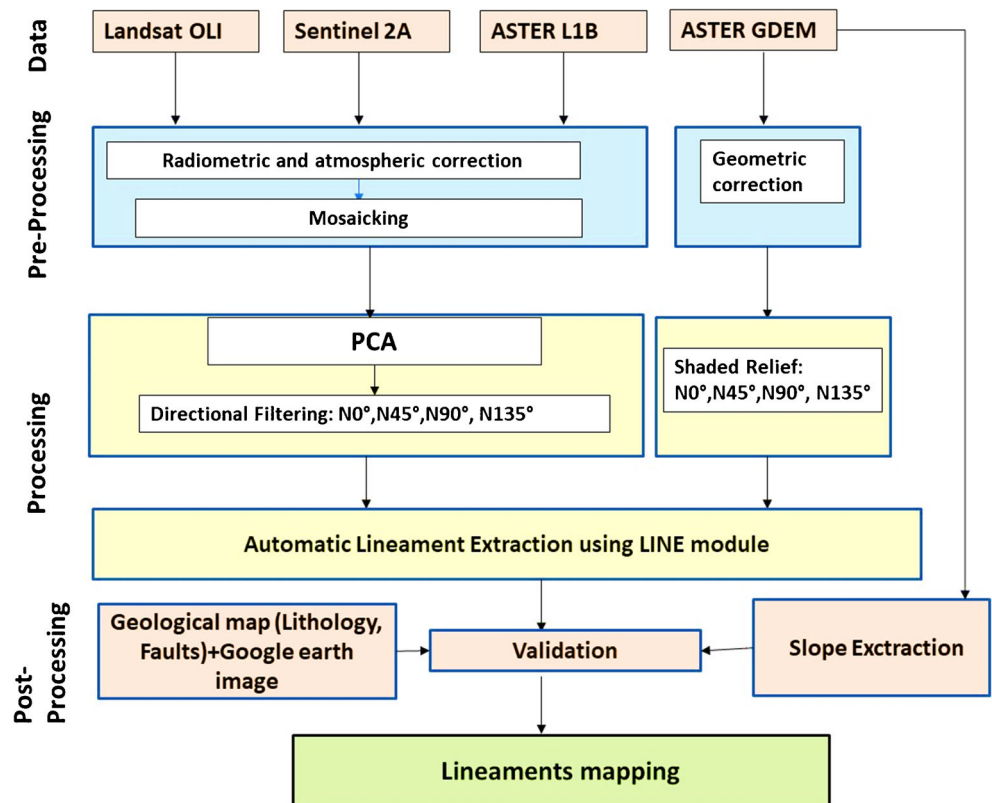
Geographically, the Rich area is located in the middle of the main road between the city of Er-Rachidia and Midelt. Geologically, this study area was located in the Eastern part

of the Central High Atlas, limited to the North by the Moulouya plain separated by faults oriented N70 to EW (Fig. 2). In the South, the study area is limited to the Anti-Atlas by the pre-Saharan furrow of Ouarzazate-Errachidia (Benammi et al. 2001). The topography of this area is diverse. It contains mountains like Mount Ayachi, which measures 3757 m in height as well as plains and high plateaus. The drainage network of the study area is crossed by high Basin of Ziz and Guir (Fig. 1).

The Central High Atlas is characterized by a thick-skinned structural style that relates to the presence of the Triassic formations that constitute the detachment level (El Harfi et al. 2006). The geomorphology of the Central High Atlas is formed by the tectonic inversion of the normal faults of the intercontinental basins by the Alpine orogeny (Babault et al. 2013; Teixell et al. 2003).

From the lithological point of view, the study zone is characterized by the Paleozoic basement in the Mougueur region, which is located 40 km East of Rich. The Mougueur Massif is composed of satin schists and sandstones-pelites of the Middle Cambrian and/or Ordovician affected by the Hercynian orogeny (Ouanaimi et al. 2018). The Mesozoic cover was initiated by Triassic formations composed of red formations and basalts that outcrop mainly at major faults (Beauchamp 1988; Ibouh 2004). The Lower Jurassic is characterized by platform formations, limestones, and dolomites, surmounted by a succession of Middle Jurassic limestones, calciturbidites, and shales (Ait Addi and Chafiki 2013; Igmoullan et al. 2001; Teixell et al. 2017). The Upper Jurassic consists of continental red formations (Ettaki et al. 2000; Haddoumi et al. 2002; Chacrone & Hamoumi 2005) underlined by marine regression, accompanied by alkaline magmatic intrusions of the Middle and Upper Jurassic

Fig. 3 Methodology flowchart of lineaments extraction



(Essaifi and Zayane 2018; Laville 1985). Lithological formations from the Cretaceous to the Tertiary are marine formations deposited generally North and South of the Central High Atlas(Michard et al. 2011)

From a structural point of view, the direction of structures in the Central High Atlas according to the study by Laville (Laville 1988) is as follows: direction faults and reverse folds is N140° and direction of normal faults and dykes is N40–50°. These structures are the result of regional senestral strike-slip fault (N70–90), which also controls the location of plutonic bodies in the region.

## Materials and methods

### Data sources

In the present work, the automatic extraction of lineaments was carried out using four types of multispectral images: Landsat OLI, ASTER, Sentinel 2A (Table 1), and ASTER-GDEM.

*Landsat- 8 OLI (Operational Land Imager)*, an American Earth observation satellite launched on 11 February 2013, consists of nine spectral bands with a spatial resolution of 30

Table 2 Results of the PCA of the used data set (x = non-used bands in the PCA)

Bands	Landsat 8		Sentinel 2		ASTER	
	Eigenvalue	Percentage	Eigenvalue	Percentage	Eigenvalue	Percentage
Band 1	385,960,231.70	98.7800	1,974,500.79	90.7800	921,255.94	94.9900
Band 2	3,739,888.35	0.9600	107,696.37	4.9500	35,748.66	3.6800
Band 3	735,517.33	0.1900	73,707.96	3.3800	8841.82	0.9100
Band 4	194,568.40	0.0490	8246.55	0.3700	3783.85	0.3900
Band 5	95,748.00	0.0240	4727.17	0.2100	99.45	0.0100
Band 6	31,017.84	0.0080	3778.68	0.1700	25.41	0.0025
Band 7	2222.56	0.0006	916.69	0.0420	14.24	0.0014
Band 8	x	x	653.83	0.0300	6.28	0.0006
Band 9	x	x	366.97	0.0160	3.88	0.0004
Band 10	x	x	322.43	0.0140	x	x

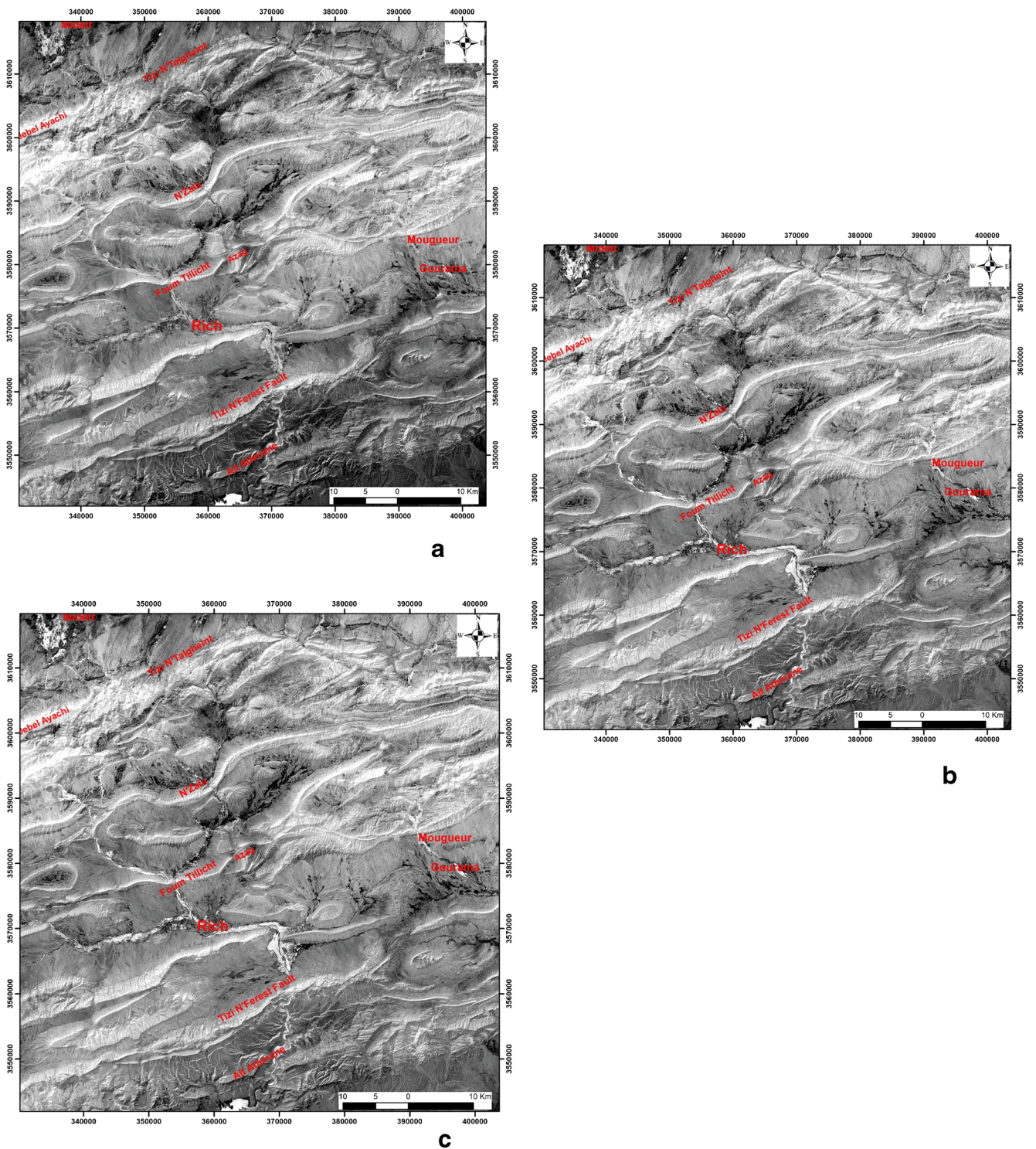


**Fig. 4** PC1 image of **A** Landsat OLI, **B** Sentinel 2A, and **C** ASTER

m for bands 1 to 7 and 9, with the exception of the panchromatic band with a spatial resolution of 15 m, and two thermal bands with a resolution of 100 m.

*ASTER (Advanced Spaceborne Thermal Emission Reflection Radiometer)* was launched in December 1999,

with three spectral bands in the visible/near-infrared (VNIR) region, six spectral bands in the short-wave infrared (SWIR) region, and five spectral bands in the thermal infrared (TIR) region with a spatial resolution of 15 m, 30 m, and 90 m respectively.

**Table 3** Matrix of weighting coefficients of the 7 × 7 directional filter for N00°, N45°, N90°, and N135°

N00°							N45°						
-1	-1	-1	0	1	1	1	-1.414214	-1.414214	-1.414214	-0.707107	0	0	0
-1	-1	-1	0	1	1	1	-1.414214	-1.414214	-1.414214	-0.707107	0	0	0
-1	-1	-1	0	1	1	1	-1.414214	-1.414214	-1.414214	-0.707107	0	0	0
-1	-1	-1	0	1	1	1	-0.707107	-0.707107	-0.707107	0	0.707107	0.707107	0.707107
-1	-1	-1	0	1	1	1	0	0	0	0.707107	1.414214	1.414214	1.414214
-1	-1	-1	0	1	1	1	0	0	0	0.707107	1.414214	1.414214	1.414214
-1	-1	-1	0	1	1	1	0	0	0	0.707107	1.414214	1.414214	1.414214
N90°							N135°						
-1	-1	-1	-1	-1	-1	-1	0	0	0	-0.707107	-1.414214	-1.414214	-1.414214
-1	-1	-1	-1	-1	-1	-1	0	0	0	-0.707107	-1.414214	-1.414214	-1.414214
-1	-1	-1	-1	-1	-1	-1	0	0	0	-0.707107	-1.414214	-1.414214	-1.414214
0	0	0	0	0	0	0	0.707107	0.707107	0.707107	0	-0.707107	-0.707107	-0.707107
1	1	1	1	1	1	1	1.414214	1.414214	1.414214	0.707107	0	0	0
1	1	1	1	1	1	1	1.414214	1.414214	1.414214	0.707107	0	0	0
1	1	1	1	1	1	1	1.414214	1.414214	1.414214	0.707107	0	0	0

*Sentinel 2A*, launched as part of the European Commission’s Copernicus program on 23 June 2015, was specifically designed to provide a large amount of data and images. The satellite is equipped with a multispectral optoelectronic sensor for surveillance with Sentinel 2A resolution of 10 to 60 m in the visible, near-infrared (VNIR) and short-wave infrared (SWIR) spectral ranges.

*Advanced Spaceborne Thermal Emission and Reflection Radiometer Global Digital Elevation Model (ASTER GDEM)* with a spatial resolution of 30 m provides topographic and hydrological information (e.g., elevation and slope and streams).

All data acquisition periods are characterized by less vegetation and snow. All images are projected in the UTM (Universal Transverse Mercator projection) coordinate system in the 30-north zone.

**Methodology**

Several techniques are used in extraction of lineaments and geomorphological features. The first step is the image pre-processing to reduce the effect of atmosphere during the avulsion of data. Then, the second step is the enhancement technique to increase the visibility of lineaments that are not delineated by the human eye (Abdullah et al. 2010). The major steps of lineament extraction are summarized in Fig. 3.

**Preprocessing**

The pre-processing of the used data consists of radiometric and atmospheric correction. Sentinel 2A images are processed in the SNAP software provided by ESA.

Then, they are resampled at 20 m and converted to ENVI format. For the ASTER and LANDSAT OLI images, after radiometric correction, the atmospheric correction of the ASTER images was performed using the FLAASH (Fast Line of-sight Atmospheric Analysis of Spectral Hypercubes) module (Gad and Kusky 2007; Pour and Hashim 2012).

**Processing**

**Principal component analysis** Principal component analysis (PCA) is an analysis method that allows the simultaneous study of a large number of variables whose total information cannot be viewed due to a space of more than three dimensions (Adiri et al. 2017; Mouissi and Alayat 2016). Principal component analysis (PCA) is commonly used in lithological mapping and lineament extraction. The aim of this step is the enhancement of the image from the reduction of noise and improved targeted information. This method is based on the mathematical transformation, which can be used to reduce the dimensionality of the data and to compress as much information in the original bands into fewer bands. This useful information for the identification of the units that exist in the image can be correctly compressed into two or three components (Sedrette and Rebaï 2016).

In this study, the principal component analysis (PCA) covariance tables indicate that the information is more concentrated in PC1 (Table 2): 98.78% 90.78%, and 94.99% for each of the Landsat OLI, ASTER, and Sentinel 2 images, respectively. Images of PC1 for the three images show that the limits of relief are very clear and the edges are very obvious (Fig. 4).

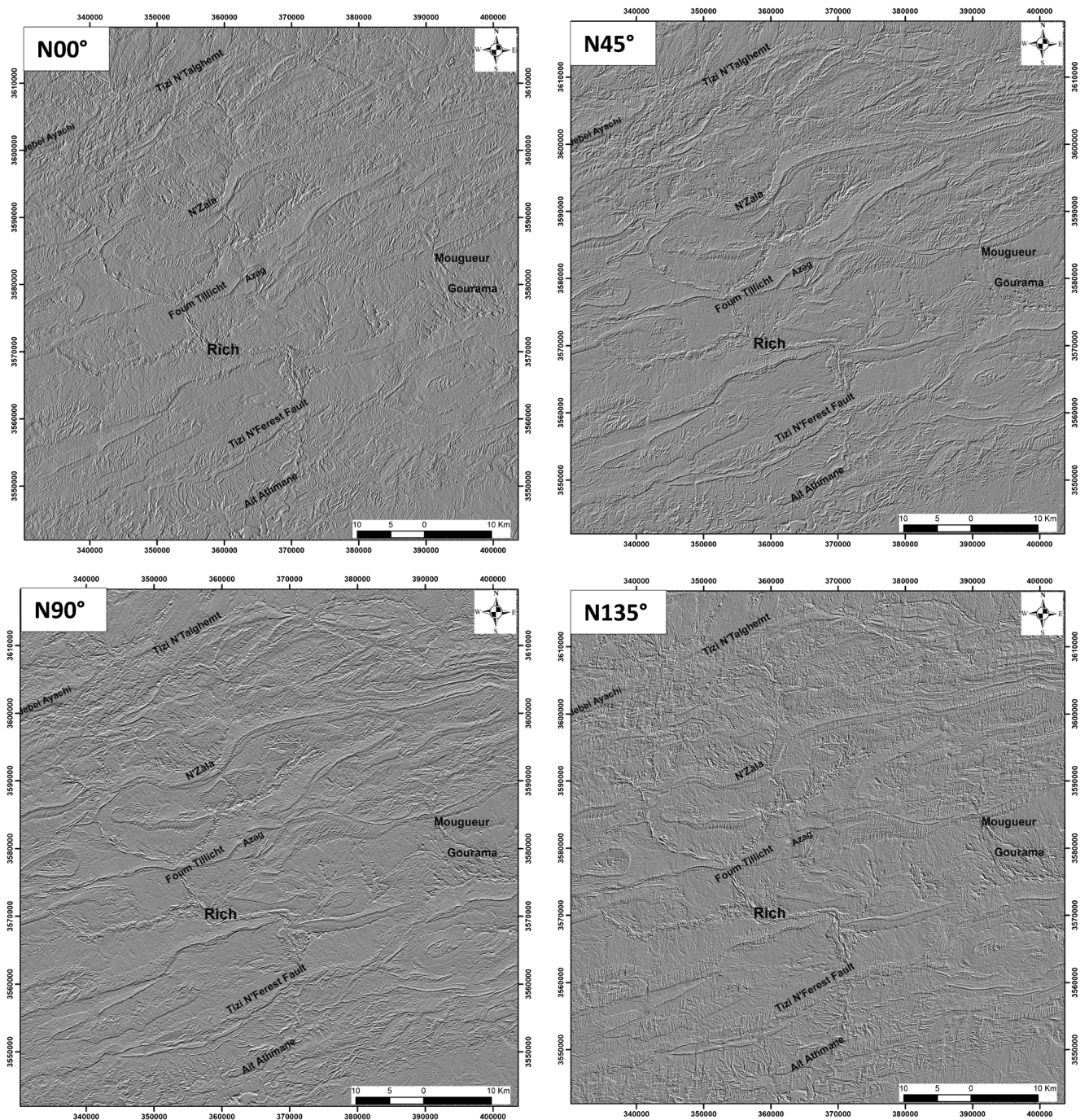


**Fig. 5** Four subset filtered images derived from PC1 of Sentinel 2 image.

**Directional filters** Directional filters are generally used for edge detection to smooth the image and reduce noise in order to improve linear structures (fractures and Faults). There are different types of filters adopted in lineament mapping (El Alaoui El Moujahid et al. 2016; Javhar et al. 2019). In this work, we applied directional filters using  $7 \times 7$  matrix in four directions ( $N0^\circ$ ,  $N45^\circ$ ,  $N90^\circ$ , and  $N135^\circ$ ) (Table 3). Each resulted filter allows detecting different orientation systems (Fig. 5).

**Shaded relief** Shaded relief is frequently used in the extraction of lineaments from DEM (Akame et al. 2013; Mallast et al. 2011). The basis of this method is to change the virtual azimuth of the sun maintaining its elevation fix, in order to create shaded relief. In the present work, the identification of the structural lineaments from the DEM image was achieved by creating four shaded relief images. Maintaining solar elevation at  $30^\circ$  we created four shaded reliefs with a solar azimuth  $0^\circ$ ,  $45^\circ$ ,  $90^\circ$ , and  $135^\circ$  (Fig. 6). The boundaries between shaded



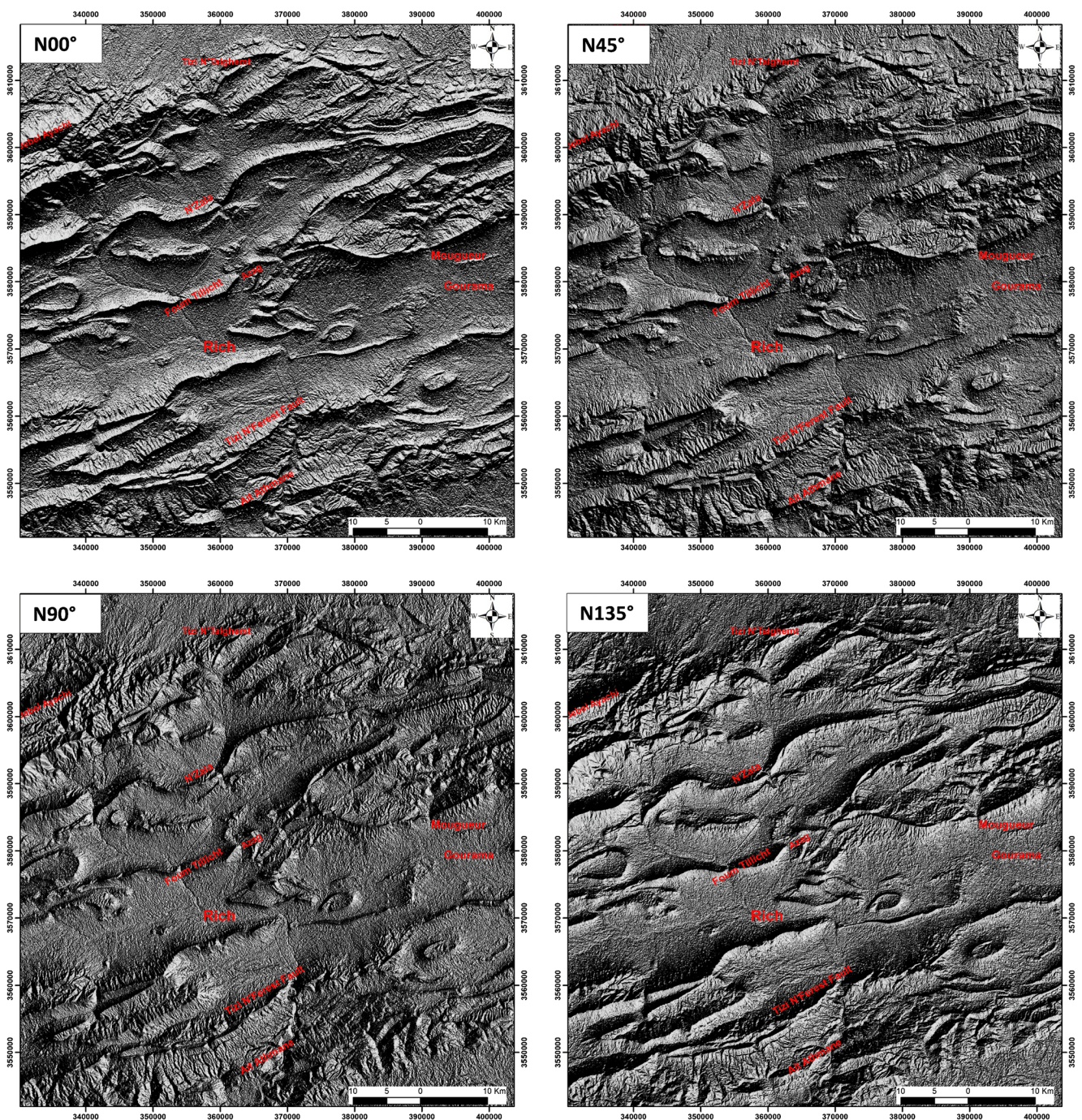


**Fig. 6** Four shaded relief images derived from DEM

and unshaded areas indicate the presence of lineaments (Abdullah et al. 2010; El Ghrabawy et al. 2019)

**Lineament extraction** The automatic extraction of the lineaments was carried out by the algorithm LINE EXTRACTION of the Geomatica software. Various parameters defined by users are needed the automatic extraction of the lineament process (Hamdani 2019; Hashim et al. 2013; Sedrette and Rebaï 2016). The process of automatic extraction of the

lineaments was applied on the four directional filter ( $N0^\circ$ ,  $N45^\circ$ ,  $N90^\circ$ , and  $N135^\circ$ ) for each of the Landsat OLI, ASTER, and Sentinel 2A images, and also the four shaded relief of DEM images ( $N0^\circ$ ,  $N45^\circ$ ,  $N90^\circ$ , and  $N135^\circ$ ). Due to the difference in spatial resolution and type of used data the definded values for automatic extraction in the algorithm are different (Table 4).

Post-processing is an essential step in lineament extraction. It consists of controlling and validating the extracted lineaments.

**Table 4** Parameters controlled the automatic extraction of the LINE module

Parameters	Signification	Range and unit
RADI (filter radius)	Radius of filter: it specifies the radius of the edge detection filter; values between 3 and 10 are recommended to avoid introducing noise	0–8192 (pixel)
LTHR Curve length threshold	It specifies the minimum length of curve to be considered as lineament (a value of 10 is suitable)	0–8192 (pixel)
FTHR line fitting threshold	It specifies the maximum error (in pixels) allowed in fitting a polyline to a pixel curve. Values between 2 and 5 are recommended.	0–8192 (pixel)
ATHR Angular difference threshold	It is the maximum angle between two vectors for them to be linked. Values between 3 and 20 are suitable	0–90
DTHR (linking distance threshold)	It specifies the minimum distance between the end points of two vectors for them to be linked. Values between 10 and 45 are acceptable	0–8192 (pixel)

The post-processing of the images was performed using ArcGIS software. First, we delete the repetitive segments. Subsequently, we delete the non-geological lineaments (River, Ridge Line,

road, rail bitumen ...) by superimposing our results to topographic and geological maps and Google Earth images and field work. Based on these steps four synthetic maps were elaborated for

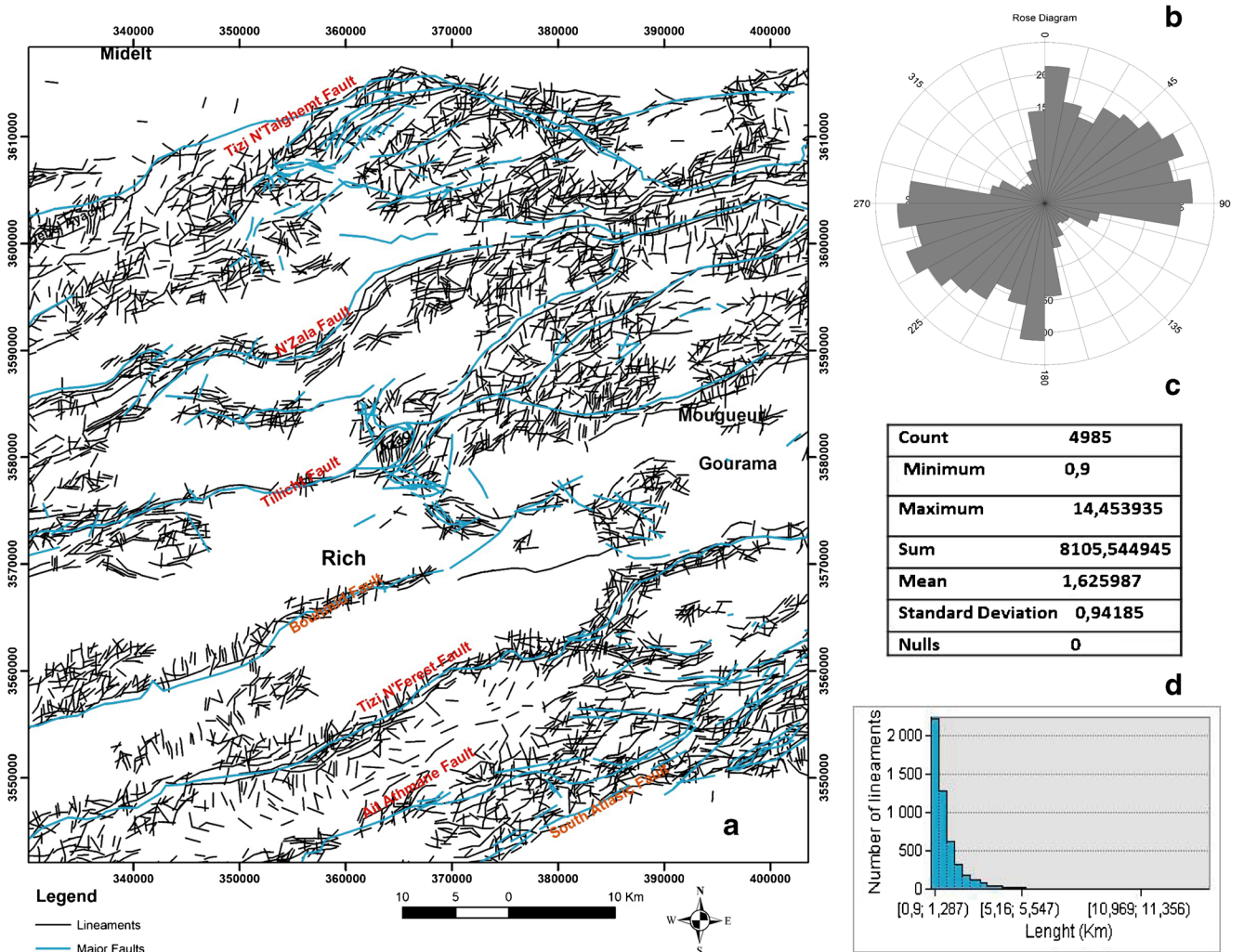


**Fig. 7** A Synthetic lineaments maps from Landsat OLI image with superposition of the results with the structural map of Ibouh (2004), and geological map of Choubert et al. (1956); **B** rose diagram of lineaments,

**C** basic statistics of automatic lineaments maps, and **D** length frequency diagram of lineaments

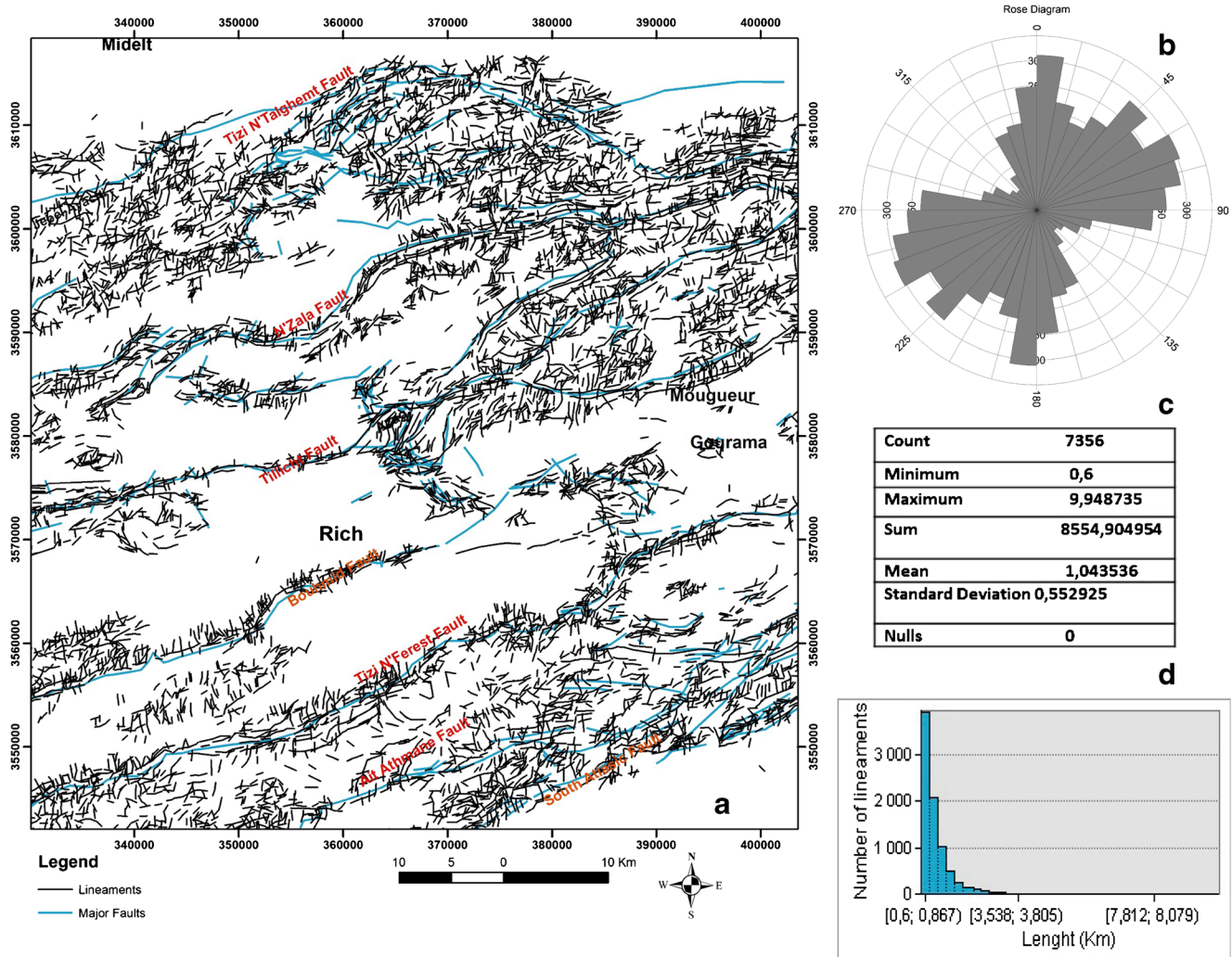


**Fig. 8** A Synthetic lineament maps from Sentinel 2 image with superposition of the results with the structural map of Ibouh (2004), and geological map of Choubert et al. (1956), **B** rose diagram of lineaments, **C** basic statistics of automatic lineament maps, and **D** length frequency diagram of lineaments

each satellite image Landsat OLI, ASTER, Sentinel 2A, and DEM (Figs. 7A, 8A, 9A, and 10A).

### Results and discussion

Statistical analysis of four types of satellite images determines a number of lineaments extracted from Landsat OLI and Sentinel 2A (images are 4985 and 7356, respectively) (Figs. 7C and 8C), while the number of lineaments extracted from ASTER and DEM images is 3940 and 4925, respectively (Figs. 9C and 10C). The results obtained show that the Sentinel 2A image allows extracting more lineaments than the others satellite images. Length frequency diagram of the Landsat OLI image shows that the length of the extracted structural lineaments is between 0.9 and 14 km (Fig. 7D) in which the majority of the extracted lineaments are between 0.9 and 1.2 km long. The length of the extracted structural lineaments from the Sentinel 2A image is between 0.6 and 9 km

(Fig. 8D) where the majority of the extracted structural lineaments are between 0.6 and 0.86 km. The length of the structural lineaments in the ASTER image is between 0.9 and 21 km (Fig. 9D), where the majority of the lineaments are between 0.9 and 1.4 km in length. The length of the structural lineaments in the DEM image is between 0.5 and 10 km (Fig. 10D) where the majority of the structural lineaments are between 0.5 and 0.6 km in length.

The results obtained by the automatic extraction of structural lineaments show the complementarity between the four types datasets, whereas the Sentinel and DEM images allow the extraction of the smallest structural lineaments, while the ASTER image allows the extraction of the longest lineaments.

The rose diagram of the Landsat OLI image shows that the main directions of the lineaments are NEE-SWW, NNE-SSW, and NE-SW (Fig. 7B). While in the direction of the lineaments in the Sentinel 2A image, the rose diagram shows that the direction of the lineaments is NEE-SWW, NNE-SSW (Fig. 8B). The direction of the lineaments according to the rose

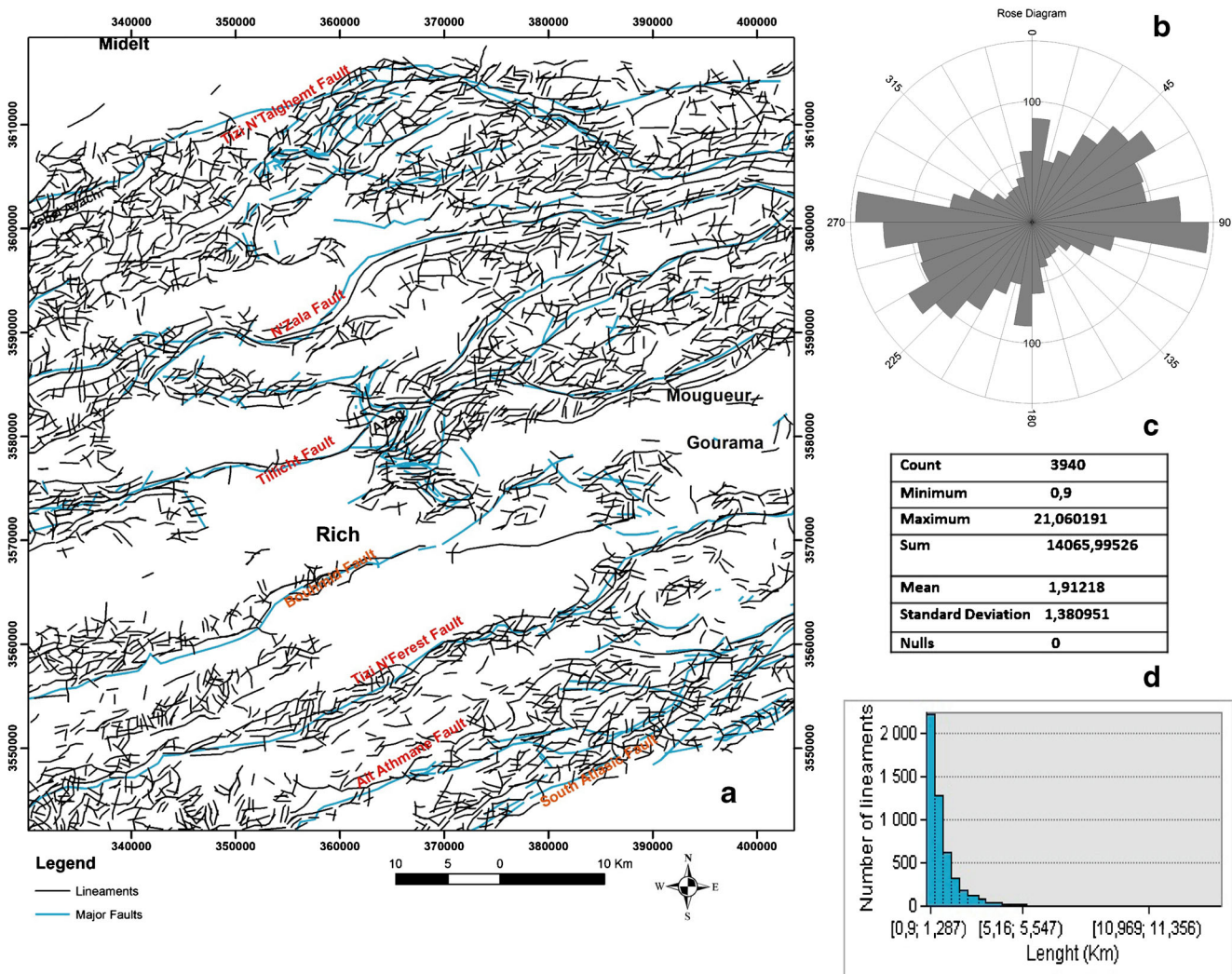


**Fig. 9** A Synthetic maps from ASTER image with superposition of the results and the structural map of Ibouh (2004), and geological map of Choubert et al. (1956), B rose diagram of lineaments, C basic statistics of automatic lineaments maps, and D length frequency diagram of lineaments

diagram of the ASTER image indicates that the direction of the lineaments is mainly NE-SW and E-W (Fig. 9B). The direction of the lineaments extracted from the DEM image presents that the direction of the lineaments are NE-SW and NEE-SWW (Fig. 10B). Lineament direction analysis results from the four satellite images are generally oriented NNE-SSW and NEE-SWW, NE-SW, and E-W.

The superposition of synthetic maps of structural lineaments shows that the fractures are grouped into families: some fractures follow the direction of major faults and others are perpendicular (Figs. 7A, 8A, 9A, and 10A).

A comparison of the fracture orientation shows a good correlation with previous work in the Central High Atlas. The Benammi seismic survey (Benammi et al. 2001) grouped the direction of the faults into three families that are N040-050, N070-090, and N110-120; these are similar to the field measurements made by Laville (1985, 1988);  $N90^\circ \pm 10^\circ E$  (E-W),  $N120^\circ \pm 10^\circ E$  (NW-SE), and  $N45^\circ \pm 10^\circ E$  (NE-SW). The work on the extraction of lineaments from spatial data in

the Central High Atlas used Landsat ETM images: the direction of the lineaments according to El Alaoui El Moujahid et al. (2016) and the main orientations are ENE-WSW, WNW-ESE, NE-SW, and NW/SE, while Nouayti et al. (2017) showed that the direction of the lineaments is from NE-SW to E-W.

The results obtained in this work indicate that the use of different satellite data by applying automatic lineament extraction makes it possible to detect different families of fractures in order to understand the influence of Alpine orogeny in the central High Atlas

### Lineament density

The analysis of lineaments density maps from Landsat OLI, Sentinel 2, ASTER, and DEM (Fig. 11) allows us to extract a common result, in which the concentration of lineaments is very high in the north-eastern part of the study area. Adding to this common result the lineament density maps of the

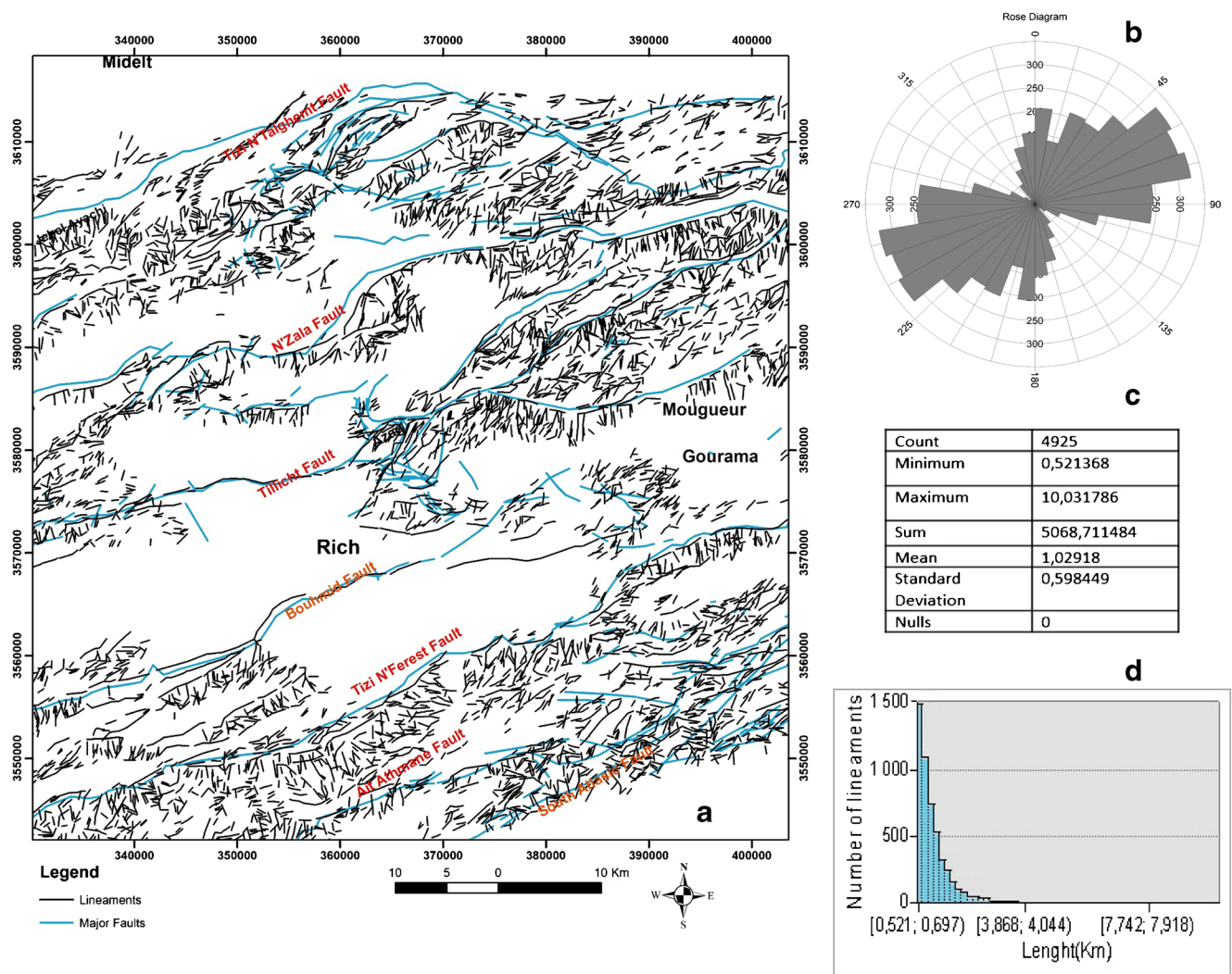


**Fig. 10** A Synthetic maps from DEM image with superposition of the results with the structural map of Ibouh (2004), and geological map of Choubert et al. (1956), B rose diagram of Lineaments. C basic statistics of automatic lineaments maps, D length frequency diagram of lineaments

Landsat OLI, Sentinel 2A, and DEM image show that the lineament concentration is remarkable between the major accidents of Tizi n’Ferst, Ait Athman, and the South Atlasic accident. However, the lineament density map of the ASTER image shows that fracturing is concentrated in the major accidents of N’zala at the Azag basin.

**Factors controlling lineament distribution**

**Geological factors**

In order to perform a geological interpretation for understanding the spatial distribution of lineaments in the study area. The superposition of the lithological map extracted from the geological map (Fig. 12) (Choubert et al. 1956; Dubar 1949) and the lineament density maps shows that the concentration of lineaments is higher in competent formations, which are

represented by platform formations including Early Jurassic limestone and dolomite.

In the study area, the concentration of structural lineaments follows the direction of major faults. This distribution of fracturing is controlled by the genesis of the Atlas chain where fracturing is decreased from East to West, in exception Jebel Ayachi. This variation is related to the rate of shortening of the Alpine orogeny (Benammi et al. 2001). Interpretation of the northeastern fracture is important in the study area due to the high overthrusting between the Tizi N’Tlghamt and N’Zala faults. Moreover, the influence of the diapirism phenomenon of the Triassic formations in the Mougueur region where the uplift of evaporitic formations favors the fracturing of carbonate rocks of Jurassic age. In the southeastern part of the study area, fracturing is related to the dynamics of the Tizi n’Ferst, Athman, and South Atlas faults.

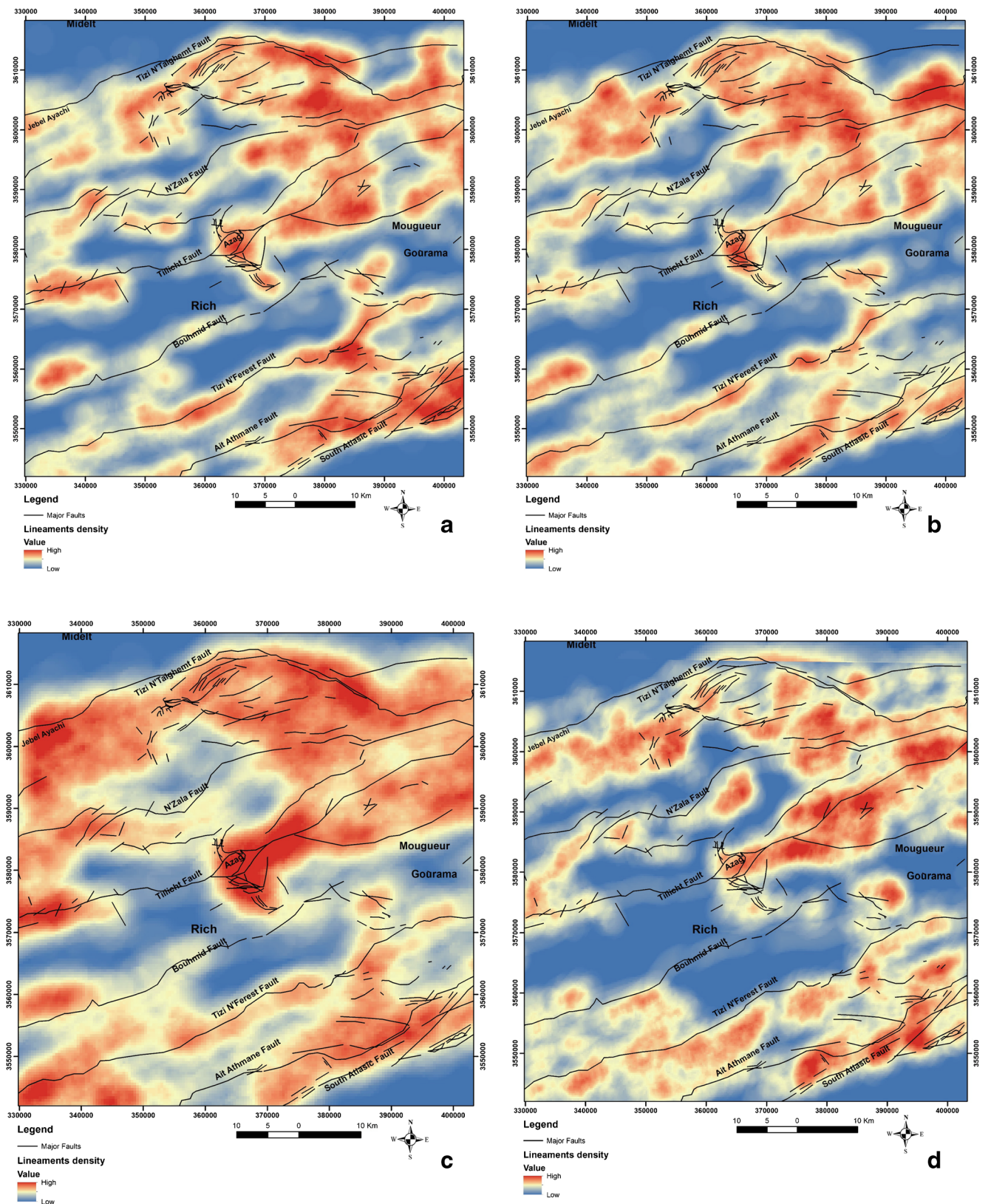


Fig. 11 Lineament density map of lineaments extract from A Landsat OLI image, B Sentinel 2A image, C ASTER image, and D DEM image

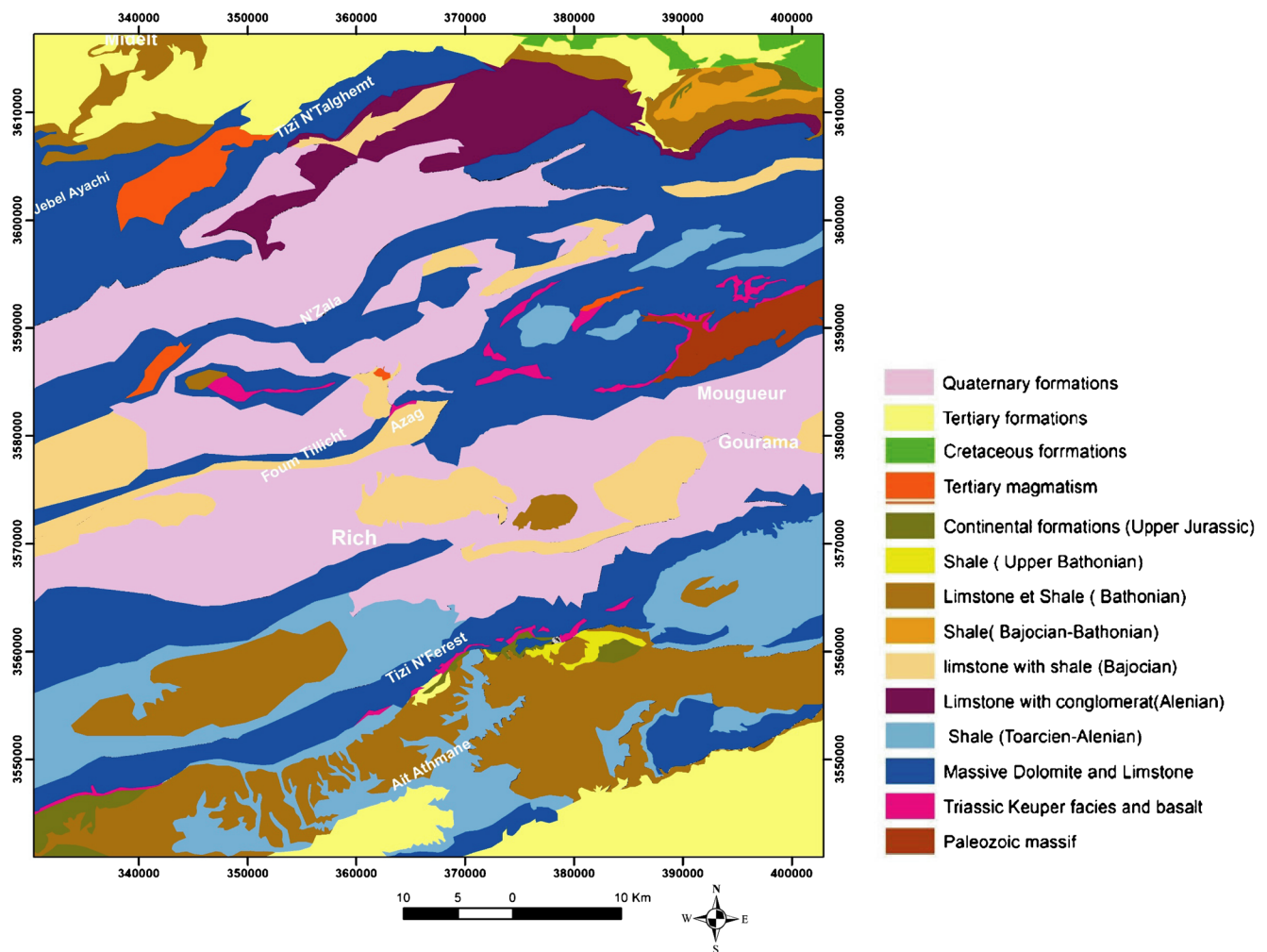


Fig. 12 Lithological map of Rich area extracted from geological map of Choubert et al. (1956) and Dubar (1949)

### Topographic factors

Slope images derived from a digital elevation (DEM) identified by a degree or a percentage (Adiri et al. 2017; Hassan and Adhab 2014). A slope map shows the topography by expressing the change in elevation where high values suggest steep slopes and low values correspond to flat areas. High values in the slope image correspond to abrupt changes, which may represent probable lineaments.

The superposition of the slope map of the DEM image and the lineaments extracted Landsat OLI, Sentinel 2, ASTER LB, and DEM (Fig. 13) shows that the concentration of lineaments is important in areas with very steep slopes; abrupt changes in values are often key indicators of the presence of linear structure.

### Final map analysis

The combination of the extracted lineaments according to the four datasets (Landsat OLI, Sentinel 2A, ASTER, and ASTER GDEM) after deleting the doubled lineaments is shown Fig.

14A. The lineament direction is mainly NE-SW, and E-W with predominance NNE-SSW and NEE-WSS (Fig. 14 B):

### Conclusion

The automatic mapping of structural lineaments minimizes the time spent in the field and gives a general idea of the dynamics of the region. In this work, four different types of images were used: Landsat OLI, ASTER, Sentinel 2A, and DEM. Following a specific methodology to extract the maximum of lineaments in order to compare and combine the results of four images. The synthetic map of structural lineaments obtained gives a detailed lineament map more than the maps obtained by conventional methods. The direction of the lineaments is grouped into families with average orientations NE-SW and E-W, with the dominance of the NNE-SSW, and NEE-WSS. Lineament distribution was controlled by the geodynamic and tectonic phases of the Alpine orogeny. This distribution of structural lineaments is related to the dynamics

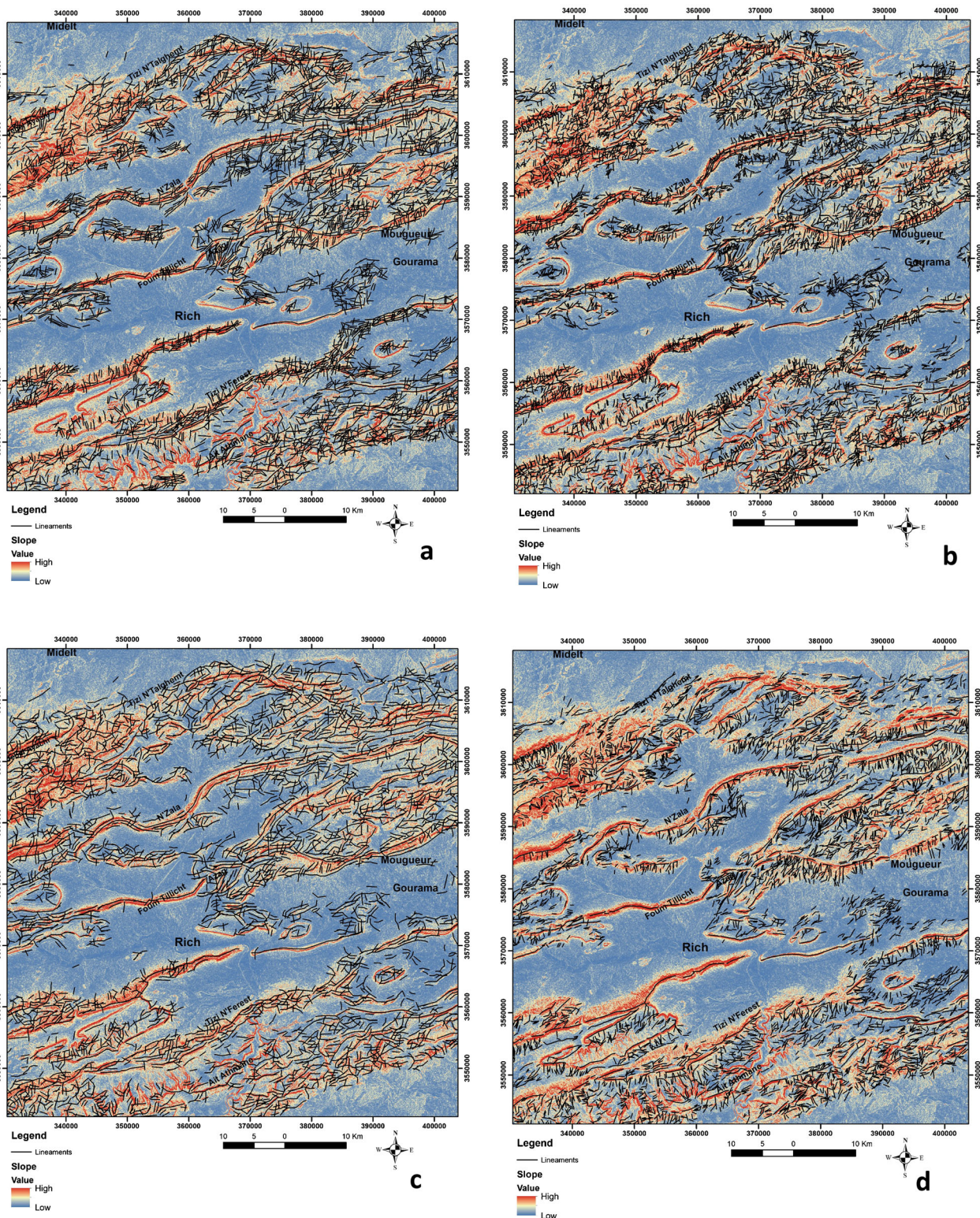


**Fig. 13** Superposition of slope image and resulted lineaments maps from **A** from Landsat OLI, **B** Sentinel 2A, **C** ASTER, and **D** DEM.

and deformation rate of the Alpine orogeny in the study area, where the concentration of lineaments is higher at major faults and the contribution of the Triassic formation phenomenon increases the fracturing of Jurassic rocks.

The results obtained in this work show the efficiency of remote sensing in mapping; it allows the extraction of structural lineaments that are difficult to detect by classical methods. The application of geostatistical methods (lineament



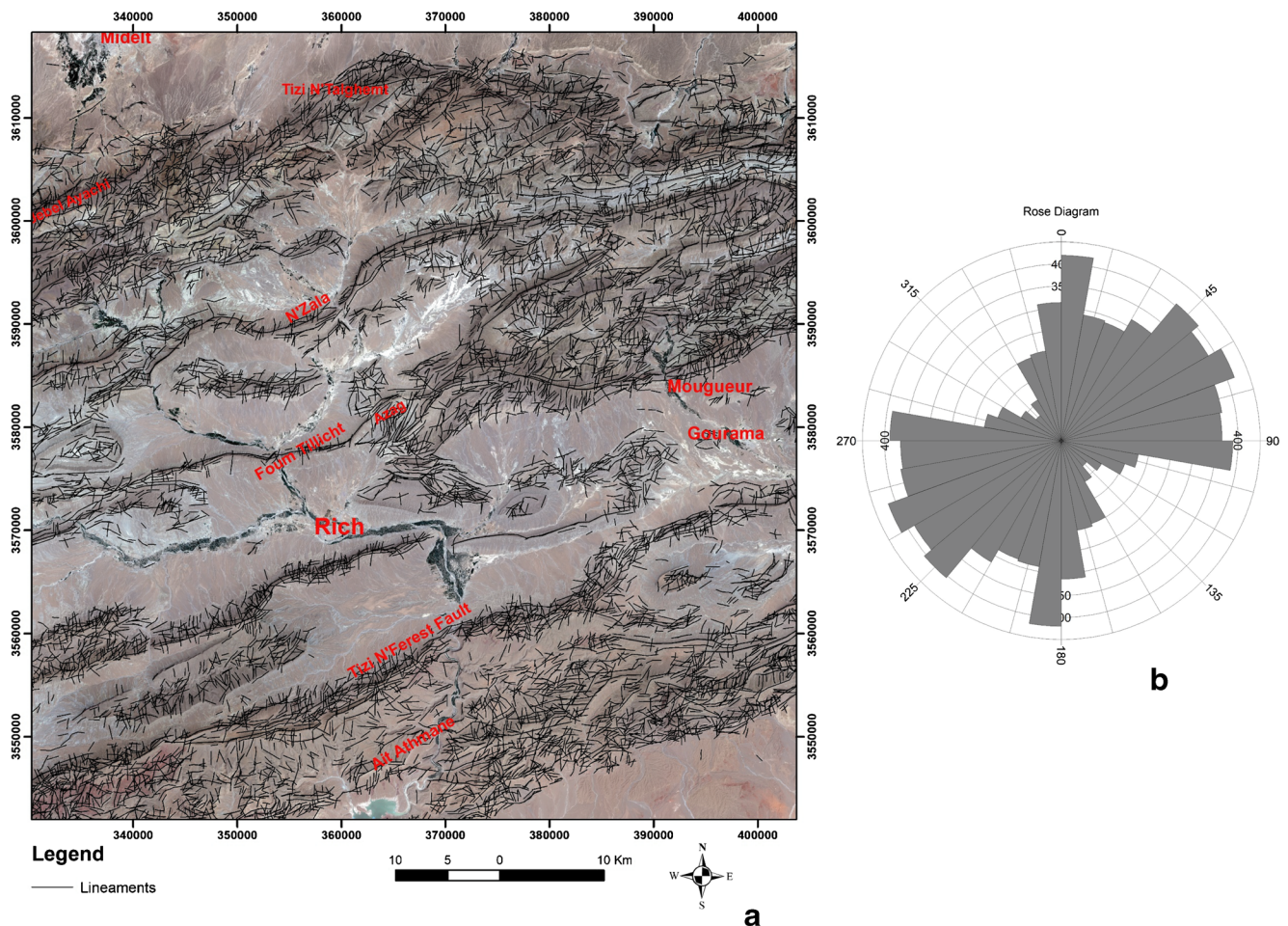


**Fig. 14** **A** Superposition of composite map of lineaments extracted from Landsat OLI, Sentinel 2A, ASTER, and DEM with RGB-321 image of Sentinel 2A. **B** Rose diagram of lineaments

density, lineament length, statistical tables) provides the researcher with several information and data to understand the geodynamics of the region. The results of this work will be useful in future research and are usable in the exploration of petroleum, groundwater, and mineralization deposits in the Central High Atlas due to the lithological and structural characteristics of the region.

**Nomenclature** PCA, Principal component analysis; OLI , Operational Land Imager; ASTER , Advanced Spaceborne Thermal Emission Reflection Radiometer; GDEM, Global Digital Elevation Model; VNIR, The visible/near-infrared; SWIR, The short-wave infrared; TIR, Thermal infrared; UTM, Universal Transverse Mercator projection; GIS, Geographic Information System

**References**

Abdullah A, Akhir JM, Abdullah I (2010) Automatic mapping of lineaments using shaded relief images derived from digital elevation model (DEMs) in the Maran - Sungi Lembing area, Malaysia. *Electron J Geotech Eng* 15(J):1–9

Adiri Z, El Harti A, Jellouli A, Lhissou R, Maacha L, Azmi M, Zouhair M, Bachaoui EM (2017) Comparison of Landsat-8, ASTER and Sentinel 1 satellite remote sensing data in automatic lineaments extraction: a case study of Sidi Flah-Bouskour inlier, Moroccan Anti Atlas. *Adv Space Res* 60(11):2355–2367. <https://doi.org/10.1016/j.asr.2017.09.006>

Ait Addi A, Chafiki D (2013) Sedimentary evolution and palaeogeography of mid-Jurassic deposits of the Central High Atlas, Morocco. *J Afr Earth Sci* 84:54–69. <https://doi.org/10.1016/j.jafrearsci.2013.04.002>

Akame JM, Mvondo Ondo J, Olinga JB, Essono J, Mbih PK (2013) Utilisation des modèles numériques de terrain (MNT) SRTM pour la cartographie des linéaments structuraux: Application à l’Archéen de Mezesse à l’est de Sangmélima (Sud-Cameroun). *Geo-Eco-Trop* 37(1):71–80

Arboleya ML, Teixell A, Charroud M, Julivert M (2004) A structural transect through the High and Middle Atlas of Morocco. *J Afr Earth Sci* 39(3–5):319–327. <https://doi.org/10.1016/j.jafrearsci.2004.07.036>

Babault J, Teixell A, Struth L, Van Den Driessche J, Arboleya ML, Tesón E (2013) Shortening, structural relief and drainage evolution in inverted rifts: insights from the Atlas Mountains, the eastern Cordillera of Colombia and the Pyrenees. *Geol Soc Spec Publ* 377(1):141–158. <https://doi.org/10.1144/SP377.14>

Beauchamp J (1988) Triassic sedimentation and rifting in the High Atlas (Morocco). In *Developments in geotectonics* (Vol. 22, Issue C).

- Elsevier B.V. <https://doi.org/10.1016/B978-0-444-42903-2.50025-7>
- Bednarik RG (2019) Rock metamorphism by kinetic energy. *Emerg Sci J* 3(5):293–302. <https://doi.org/10.28991/esj-2019-01192>
- Benammi M, Arbi Toto E, Chakiri S et al (2001) Les chevauchements frontaux du Haut Atlas central marocain: Styles structuraux et taux de raccourcissement différentiel entre les versants nord et sud. *CR Acad Sci Paris* 333(4):241–247. [https://doi.org/10.1016/S1251-8050\(01\)01628-7](https://doi.org/10.1016/S1251-8050(01)01628-7)
- Chacrone C, Hamoumi N (2005) L’Arenig-Llanvirn du Haut Atlas occidental et central (Maroc). Environnements sédimentaires, paléogéographie et contrôle de la sédimentation. *Compt Rendus Geosci* 337(12):1026–1034. <https://doi.org/10.1016/j.crte.2005.05.015>
- Choubert G, Dubar G, Hindermeyer J (1956) Carte géologique du Haut Atlas au nord Ksares Souk et de Boudnib: Feuilles Riche et Boudnib au 1/200 000. Notes et Mémoires Du Service Géologique Du Maroc, N°81
- Dormishi A, Ataei M, Mikaeil R, Khalo Kakaei R (2018) Relations between texture coefficient and energy consumption of Gang Saws in carbonate rock cutting process. *Civil Eng J* 4(2):413. <https://doi.org/10.28991/cej-0309101>
- Dubar G (1949) Carte géologique provisoire du Haut Atlas de Midelt au 1/200 000. Notes et Mémoires Du Service Géologique Du Maroc, N°59bis
- El Alaoui El Moujahid H, Ibouh H, Bachnou A, Babram MA, El Harti A (2016) Mapping and analysis of geological fractures extracted by remote sensing on Landsat TM images, example of the Imilchil-Tounfite area (central High Atlas, Morocco). *Estud Geol* 72(2): 051. <https://doi.org/10.3989/egol.42328.394>
- Ghrabawy O El, Soliman N, Tarshan A (2019) Remote sensing signature analysis of ASTER imagery for geological mapping of Gasus area , central eastern desert , Egypt
- El Harfi A, Guiraud M, Lang J (2006) Deep-rooted “thick skinned” model for the High Atlas Mountains (Morocco). Implications for the structural inheritance of the southern Tethys passive margin. *J Struct Geol* 28(11):1958–1976. <https://doi.org/10.1016/j.jsg.2006.08.011>
- Essaifi A, Zayane R (2018) Petrogenesis and origin of the Upper Jurassic-Lower Cretaceous magmatism in Central High Atlas (Morocco): Major, trace element and isotopic (Sr-Nd) constraints. *J Afr Earth Sci* 137:229–245. <https://doi.org/10.1016/j.jafrearsci.2017.10.002>
- Ettaki M, Chellaï EH, Milhi A, Sadki D, Boudchiche L (2000) Le passage Lias moyen-Lias supérieur dans la région de Todra-Dadès : événements bio-sédimentaires et géodynamiques (Haut Atlas central, Maroc). *Comptes Rendus de l’Académie Des Sciences - Series IIA - Earth and Planetary Science*, 331(10), 667–674. [https://doi.org/10.1016/s1251-8050\(00\)01458-0](https://doi.org/10.1016/s1251-8050(00)01458-0)
- Gad S, Kusky T (2007) ASTER spectral ratioing for lithological mapping in the Arabian-Nubian shield, the Neoproterozoic Wadi Kid area, Sinai, Egypt. *Gondwana Res* 11(3):326–335. <https://doi.org/10.1016/j.gr.2006.02.010>
- Haddoumi H, Charrière A, Feist M, Andreu B (2002) Nouvelles datations (Hauterivien supérieur-Barrémien inférieur) dans les «Couches rouges» continentales du Haut Atlas central marocain ; conséquences sur l’âge du magmatisme et des structurations mésozoïques de la chaîne Atlasique. *Comptes Rendus Palevol* 1(5):259–266. [https://doi.org/10.1016/S1631-0683\(02\)00039-8](https://doi.org/10.1016/S1631-0683(02)00039-8)
- Hamdani N (2019) Fracture network mapping using Landsat 8 OLI data and linkage with the Karst system: a case study of the Moroccan Central Middle Atlas
- Hashim M, Ahmad S, Johari MAM, Pour AB (2013) Automatic lineament extraction in a heavily vegetated region using Landsat Enhanced Thematic Mapper (ETM+) imagery. *Adv Space Res* 51(5):874–890. <https://doi.org/10.1016/j.asr.2012.10.004>
- Hassan MA, Adhab SS (2014) Lineament automatic extraction analysis for Galal Badra river basin using Landsat 8 satellite image. *Iraqi Journal of Physics* 12(25):55–44
- Ibouh H (2004) Du rift avorté au bassin sur décrochement, contrôles tectonique et sédimentaire pendant le Jurassique (Haut Atlas central, Maroc). Université de Marrakech, Maroc
- Igmoullan B, Sadki D, Fedan B, Chellai EH (2001) Evolution géodynamique du Haut-Atlas de Midelt ( Maroc ) pendant le Jurassique: un exemple d’interaction entre la tectonique et l’eustatisme. *Bulletin de l’Institut Scientifique* 23(October 2014): 47–54
- Javhar A, Chen X, Bao A, Jamshed A, Yunus M, Jovid A, Latipa T (2019) Comparison of multi-resolution optical Landsat-8, Sentinel-2 and radar Sentinel-1 data for automatic lineament extraction: A case study of Alichur area, SE Pamir. *Remote Sens* 11(7):1–29. <https://doi.org/10.3390/rs11070778>
- Kassou A, Essahlaoui A, Aissa M et al (2012) Extraction of structural lineaments from satellite images Landsat 7 ETM+ of Tighza Mining District (Central Morocco). *Res J Earth Sci* 4(2):44–48. <https://doi.org/10.5829/idosi.rjes.2012.4.2.1110>
- Kumar S, Bhandary T (2015) Comparative study of Landsat and Aster data by morphometric analysis. *Civil Eng J* 1(2):21–25. <https://doi.org/10.28991/cej-2015-00000007>
- Laville E (1985) Evolutions sédimentaire, tectonique et magmatique du bassin jurassique du Haut Atlas (Maroc) : modèles en relais multiple de décrochements. Univ. Montpellier, France
- Laville E (1988) A multiple releasing and restraining stepover model for the Jurassic strike-slip basin of the Central High Atlas (Morocco). In *Developments in Geotectonics* (Vol. 22, Issue C). Elsevier B.V. <https://doi.org/10.1016/B978-0-444-42903-2.50026-9>
- Mafi Gholami D, Baharlouii M (2019) Monitoring long-term mangrove shoreline changes along the Northern Coasts of the Persian Gulf and the Oman Sea. *Emerg Sci J* 3(2):88. <https://doi.org/10.28991/esj-2019-01172>
- Mallast U, Gloaguen R, Geyer S (2011) Derivation of groundwater flow-paths based on semi-automatic extraction of lineaments from remote sensing data. 2665–2678. <https://doi.org/10.5194/hess-15-2665-2011>
- Michard A, Ibouh H, Charrière A (2011) Syncline-topped anticlinal ridges from the High Atlas: a Moroccan conundrum, and inspiring structures from the Syrian Arc, Israel. *Terra Nova* 23(5):314–323. <https://doi.org/10.1111/j.1365-3121.2011.01016.x>
- Mouissi S, Alayat H (2016) Utilisation de l’Analyse en Composantes Principales (ACP) pour la Caractérisation Physico-Chimique des Eaux d’un Ecosystème Aquatique: Cas du Lac Oubéira (Extrême NE Algérien). *J Mater Environ Sci* 7(6):2214–2220
- Nouayti N, Khattach D, Hilali M (2017) Cartographie des zones potentielles pour le stockage des eaux souterraines dans le haut bassin du Ziz (Maroc): Apport de la télédétection et du système d’information géographique. *Bulletin de l’Institut Scientifique, Section Sciences de La Terre* 39:45–57
- Oo MM, Kyi CCT, Zin WW (2019) Historical morphodynamics assessment in bridge areas using remote sensing and GIS techniques. *Civil Eng J* 5(11):2515–2524. <https://doi.org/10.28991/cej-2019-03091429>
- Ouanaimi H, Soulaïmani A, Baïdder L, Eddebbi A, Hoepffner C (2018) Unraveling a distal segment of the West African Craton Paleozoic margin: stratigraphy of the Mougeur inlier of the eastern High Atlas, Morocco. *Compt Rendus Geosci* 350(6):289–298. <https://doi.org/10.1016/j.crte.2018.06.008>
- Pour AB, Hashim M (2012) Identifying areas of high economic-potential copper mineralization using ASTER data in the Urumieh-Dokhtar Volcanic Belt, Iran. *Adv Space Res* 49(4):753–769. <https://doi.org/10.1016/j.asr.2011.11.028>
- Sedrette S, Rebaï N (2016) Automatic extraction of lineaments from Landsat Etm+ images and their structural interpretation: Case

- Study in Nefza region (North West of Tunisia). *J Res Environ Earth Sci* 2018:139–145 <http://earthexplorer.usgs.gov>
- Si Mhamdi H, Raji M, Oukassou M (2016) Utilisation de la Télédétection dans la Cartographie Automatique des Linéaments Géologiques du Granitoïde de Tichka ( Haut Atlas Occidental ). *142*(4), 321–333
- Si Mhamdi H, Raji M, Maimouni S, Oukassou M (2017) Fractures network mapping using remote sensing in the Paleozoic massif of Tichka (Western High Atlas, Morocco). *Arab J Geosci*, 10(5). <https://doi.org/10.1007/s12517-017-2912-5>
- Teixell A, Arboleya ML, Julivert M, Charroud M (2003) Tectonic shortening and topography in the central High Atlas (Morocco). *Tectonics* 22(5). <https://doi.org/10.1029/2002TC001460>
- Teixell A, Barnolas A, Rosales I, Arboleya ML (2017) Structural and facies architecture of a diapir-related carbonate minibasin (lower and middle Jurassic, High Atlas, Morocco). *Mar Pet Geol* 81:334–360. <https://doi.org/10.1016/j.marpetgeo.2017.01.003>